Multisensor Data-Fusion-Based Approach to Airspeed Measurement Fault Detection for Unmanned Aerial Vehicles

Dingfei Guo, Maiying Zhong, and Donghua Zhou, *Senior Member, IEEE*

***Abstract*— Fault detection (FD) plays an important role in guaranteeing system safety and reliability for unmanned aerial vehicles (UAVs). This paper focuses on developing an alternative approach to FD for airspeed sensor in UAVs by using data from gyros, accelerometers, global positioning system, and wind vanes. Based on the kinematics model of the UAV, an estimator is proposed to provide analytical redundancy using information from the above-mentioned sensors, which are commonly implemented on UAVs. This filter process is independent of the airspeed measurement and the aircraft dynamics model. Furthermore, we employ the observability rank criterion based on Lie derivatives and prove that the nonlinear system describing the airspeed kinematics is observable. The χ^2 test and cumulative sum detector are employed to detect the occurrence of airspeed measurement faults together. Finally, the performance of the proposed methodology has been evaluated through flight experiments of UAVs.**

***Index Terms*— Airspeed estimation, fault detection (FD), kinematics model, pitot tube, unmanned aerial vehicle (UAV).**

I. Introduction

THE mobility and economic efficiency of unmanned aerial vehicles (UAVs) provide them with a high number of applications [1]. A UAV is a typical multisensor system, including inertial measurement unit (IMU), global positioning system (GPS), air data system (ADS), magnetometer, and so forth. To achieve precise control and navigation of the UAV, the reliability of the sensor system must be ensured. One of the most important sensors is the pitot tube, which provides information about the airspeed. The standard method for determining airspeed is to calculate the airspeed using the dynamic pressure measured from a pressure sensor connected to a pitot tube. This sensor is very exposed because of its position in the airstream, and it can easily be clogged by dust or water particles that freeze at higher altitudes when they come into contact with the airplane body. Pitot tube defects can have catastrophic consequences for airplanes, particularly UAVs, which do not have the same sensor redundancy that is available on larger aircraft. Thus, fault detection (FD) and isolation techniques that incorporate analytical redundancy are favored.

A general approach for airspeed sensor FD is hypothesis testing of the innovation [2]. Dating back to the 1970s, the use of analytical redundancy was employed for sensor failure identification, as reported in [3], for example. In that work, a bank of so-called "sequential probability ratio tests" computed the probabilities on whether a sensor was faulty over a time window of residuals. Other innovation tests were performed, e.g., chi-square tests in [4] or the Tracy–Widom distribution test in [5]. However, these approaches cannot isolate airspeed sensor faults from actuator or other sensor faults. Another technique is the multiple model adaptive estimation technique [6] based on an idea from [7]. This technique is based on a bank of parallel Kalman filters, each of which matches a particular fault status of the system or any one sensor/actuator. However, this approach requires *a priori* statistical characteristics of faults that occurred in the system. In practice, such information is mostly not available, and using this approach has limited applications for airspeed FD. Moreover, fault estimation [11] can hardly be used for UAVs because of the same limitations. As an alternative to innovation tests from Kalman filters, airspeed estimation is employed to generate a residual signal for detecting potential pitot tube faults. Reference [13] utilized stereo vision to measure the velocity of vehicles. Reference [14] estimated the airspeed from the throttle setting to detect failures on the pitot tube onboard a small UAV. Another approach by Cho *et al.* [15] developed an airspeed estimation algorithm using a Kalman filtering technique based on the geometric relationship among the airspeed, wind speed, and ground speed of a UAV. Combining the above-mentioned two airspeed estimations and airspeed measurements, [16] provided a detailed fault diagnosis analysis for the airspeed sensor. However, these approaches suffer from a few limitations. They require the use of the pitot tube information to estimate the wind or unknown parameters, which are then used to estimate the airspeed; therefore, these airspeed estimations cannot be considered to be independent of the pitot tube. Reference [10] proposed a practical approach for estimating the airspeed of a UAV based only on the nonlinear equations regulating the dynamics of the aircraft angle of attack. The authors assumed the exact knowledge of the inertial, geometric, aerodynamic, and thrust modeling parameters of the UAV, resulting in a quadratic equation of the airspeed. Although an explicit aircraft model is required,

Manuscript received March 9, 2017; revised May 19, 2017; accepted July 8, 2017. Date of publication December 6, 2017; date of current version January 4, 2018. This work was supported in part by the National Natural Science Foundation of China under Grant 61333005, Grant 61210012, and Grant 61421063, and in part by the Research Fund for the Taishan Scholar Project of Shandong Province of China. The Associate Editor coordinating the review process was Dr. Yong Yan. *(Corresponding author: Maiying Zhong.)*

D. Guo is with the School of Instrumentation Science and Opto-electronic Engineering, Beihang University, Beijing 100191, China.

M. Zhong and D. Zhou are with the College of Electrical Engineering and Automation, Shandong University of Science and Technology, Qingdao 266590, China (e-mail: myzhong@buaa.edu.cn).

Color versions of one or more of the figures in this paper are available online at http://ieeexplore.ieee.org.

Digital Object Identifier 10.1109/TIM.2017.2735663

0018-9456 © 2017 IEEE. Personal use is permitted, but republication/redistribution requires IEEE permission.
See http://www.ieee.org/publications_standards/publications/rights/index.html for more information.

the trained model may contain aircraft-specific information in its parameters; therefore, it can only be used for the specific UAV for which it has been identified. Reference [12] used rate-gyro, accelerometer, GPS, angle of attack, and sideslip measurements to estimate the velocity relative to the air. The advantage of this type of approach is that it can be implemented on any aircraft without the need for aircraft modeling or tuning of the modeling uncertainties. However, the observability of attitude estimation cannot be proven.

In this paper, an alternative approach is proposed for airspeed sensor FD using the frequently used sensors in the UAV. Different from the hypothesis testing of the innovation-based FD, this approach uses the difference between the airspeed estimation and the airspeed measurement to indicate the pitot tube fault. Therefore, a pitot-tube-independent estimation for airspeed is presented using the extended Kalman filter (EKF) first. A sensing system using this approach can be moved from one aircraft to another without requiring any changes to the filter, except for tuning for different sensors. Note that the accurate attitude of an aircraft is important for the airspeed estimation. In this paper, an all error state inertial navigation system (INS)/GPS integration algorithm is chosen to estimate the attitude errors, which can be used to correct the INS attitudes and other uncertainties. At the same time, based on the observability analysis of the INS/GPS integrated system [22], a comprehensive observability of the system using the Lie derivative [20] is formed to ensure that the sensor measurements provide sufficient information. In the FD scheme, the performance of the used sensors, i.e., IMU, GPS, and wind vanes, is a key component guaranteeing the reliability of the FD. Therefore, health monitoring of these sensors need to be implemented all times. Before the pitot tube FD, this paper uses a χ^2 test to determine whether these sensors work regularly. Based on the health monitoring, a cumulative sum (CUSUM) test [24] is used to detect airspeed sensor fault.

The remainder of this paper is structured as follows. In section II, we give the problem statement. Section III presents the method for estimating airspeed using a GPS receiver, IMU, and wind vanes. Airspeed sensor FD is detailed in Section IV. Finally, the proposed approach is validated using actual flight data from the Thor UAV, based on the Ultra Stick platform from the University of Minnesota.

II. Problem Statement

The basic relationships between the airspeed measurement and UAV states are derived in [25]. For simplicity, based on Bernoulli's equation, the airspeed can be expressed as follows:

$$V = K\sqrt{\frac{2(P_t - P_s)}{\rho}} = K\sqrt{\frac{2P_d}{\rho}} \tag{1}$$

where V is the airspeed to be measured; P_t is the total pressure; P_s is the static pressure; P_d is the difference between the total pressure and the static pressure, i.e., the dynamic pressure; ρ is the fluid density; and K is a correction factor. In many UAVs, pitot tubes are used to measure dynamic pressure, which can be used to calculate airspeed.

Pitot tube failures have resulted in several fatal accidents for commercial, military, and general UAVs. The traditional approach to sensor fault tolerance is hardware redundancy [2]. Multiple hardware components provide protection against damage. Such schemes operate in triple or quadruple redundancy configurations. However, for small UAV systems, hardware redundancy approaches cannot simultaneously achieve high performance and high reliability. In addition, failures on any individual pitot tube are also likely to occur on other pitot tubes under certain weather conditions, resulting in common-mode failures.

An alternative to hardware redundancy is analytical redundancy, in which health-monitoring software uses a system process model to generate residuals. Common techniques for residual generation, such as [3]–[5], utilize analysis of Kalman filtering-based innovations within a statistical framework. The residual should be a good representation of the fault and insensitive to process and measurement noises, and it is expressed as follows:

$$\tilde{y} = y - \hat{y} \tag{2}$$

where y stands for measurements from sensors of the UAV, including airspeed, locations, wind angles, and angular rates. $\hat{y}$ is the estimated measurement using EKF [4] or other H_∞-type filters [8], [9]. $\tilde{y}$ is the generated residual. Based on the analysis of the residual (2), FD of the airspeed sensor is properly implemented. However, there are a few limitations in these innovation-based approaches. First, these approaches cannot distinguish pitot tube faults from other sensor faults, because this residual $\tilde{y}$ also includes other sensors' information. Moreover, they are strong-model-based methods in the sense that complete knowledge on the characteristics of the signals and the underlying dynamics is required. These structures cannot provide good cross-platform portability.

To overcome these shortcomings, this paper presents an alternative model-independent method to detect and isolate the airspeed sensor fault. A general diagram of this approach is shown in Fig. 1. Several regularly available sensors, i.e., IMU, GPS, and wind vanes, are used to estimate the "virtual airspeed," which is independent of the "physical airspeed" from the pitot tube. The detection of a failed physical pitot tube is based on monitoring of the residual between the signal obtained via the physical sensor and its estimated counterpart. This residual can be expressed as follows:

$$r = V_m - \hat{V} \tag{3}$$

where V_m is the absolute value of the airspeed measurement, $\hat{V}$ is the absolute value of the estimated airspeed, and r is the residual that only includes the airspeed information. In Section III, we will present the formulation of the airspeed estimation.

III. Airspeed Estimation Formulation

A. System Description

Before developing the aircraft equations of motion, it is necessary to define reference frames and sign conventions. All reference frames are right handed with mutual orthogonal axes.

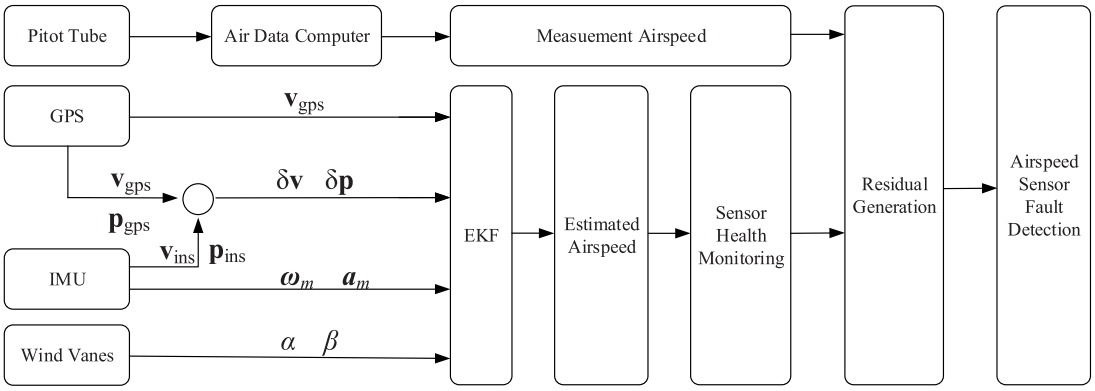

Fig. 1. General diagram of FD scheme.

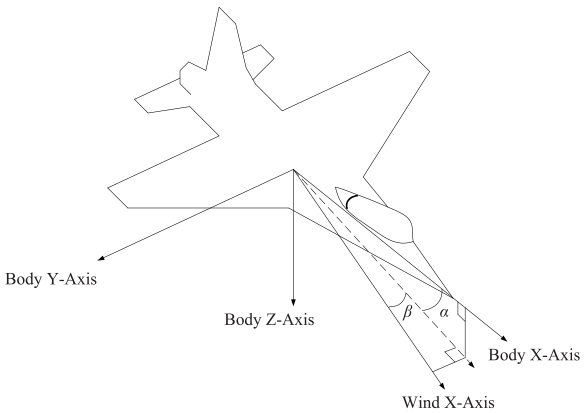

Fig. 2. Relationship between aircraft body and wind frames.

The inertial frame (i frame) has its origin at the center of the earth and not rotating with the fixed stars. The local-level north-east-down (NED) frame is selected as the navigation frame (n frame).

The body frame (b frame) is $x_b y_b z_b$. The origin is at the aircraft center of gravity, with the positive x_b-axis pointing forward through the nose of the aircraft, the positive y_b-axis out of the right wing, and the positive z_b-axis through the underside.

The wind axes are $X_w Y_w Z_w$. The origin is at the aircraft center of gravity, with the positive X_w-axis being forward and aligned with the air-relative velocity vector, the positive Y_w-axis out of the right side of the aircraft, and the positive Z_w-axis through the underside in the $X_w Y_w$ plane in the body axes. Fig. 2 shows the relationship between the aircraft body frame and the wind frame using the attack angle α and the sideslip angle β.

The estimation is available through exploiting the dynamics in component form [23]

$$\begin{bmatrix} \dot{u} \\ \dot{v} \\ \dot{w} \end{bmatrix} = \begin{bmatrix} 0 & r & -q \\ -r & 0 & p \\ q & -p & 0 \end{bmatrix} \begin{bmatrix} u \\ v \\ w \end{bmatrix} + C_n^b \begin{bmatrix} 0 \\ 0 \\ g \end{bmatrix} + \frac{1}{m} \begin{bmatrix} F_{Ax} + F_T \\ F_{Ay} \\ F_{Az} \end{bmatrix} \tag{4}$$

where $\mathbf{V}_a = [u \ v \ w]^T$ denotes the body-axis airspeed components; Euler attitude angles $\mathbf{\Phi} = [\phi \ \theta \ \psi]^T$ stand for roll, pitch, and yaw, respectively; and C_n^b is the attitude transformation matrix between the b frame and the n frame

$$C_n^b = \begin{bmatrix} \cos\psi\cos\theta & \sin\psi\cos\theta & -\sin\theta \\ \cos\psi\sin\theta\sin\phi - \sin\psi\sin\phi & \cos\psi\cos\phi + \sin\phi\sin\theta\sin\phi & \cos\theta\sin\phi \\ \cos\psi\sin\theta\cos\phi + \sin\psi\sin\phi & \sin\psi\sin\theta\cos\phi - \cos\psi\sin\phi & \cos\theta\cos\phi \end{bmatrix}. \tag{5}$$

Here, g is local gravitational acceleration; p, q, and r denote the body-axis projections of angular velocity; and m is the constant mass of the UAV. The aerodynamic forces are F_{Ax}, F_{Ay}, and F_{Az}, and F_T is the thrust force.

Equation (4) provides the dynamic equation of the UAV. Aerodynamic forces acting on the aircraft result from the relative motion of the air and the aircraft. Components of the aerodynamic forces can be expressed in terms of nondimensional coefficients and dynamic pressure. Generally, modern computational methods and wind-tunnel testing can provide, in many instances, comprehensive data about the aerodynamic characteristics of an aircraft. In this paper, an IMU is used to measure accelerations and angular rates

$$\begin{aligned} \boldsymbol{a}_m &= \frac{1}{m}[F_{Ax} + F_T \quad F_{Ay} \quad F_{Az}]^T \\ \boldsymbol{\omega}_m &= [p \quad q \quad r]^T \end{aligned} \tag{6}$$

where $\boldsymbol{a}_m$ and $\boldsymbol{\omega}_m$ are the outputs of accelerometers and rate gyroscopes, respectively. There are multiple possible sources of error in the accelerometer and rate gyroscope measurements, such as calibration errors, alignment errors, and sensor noise, which can be modeled as

$$\begin{aligned} \boldsymbol{a}_m &= \boldsymbol{a} + \nabla + \boldsymbol{W}^{\boldsymbol{a}} \\ \boldsymbol{\omega}_m &= \boldsymbol{\omega} + \boldsymbol{\varepsilon} + \boldsymbol{W}^{\boldsymbol{\omega}} \end{aligned} \tag{7}$$

where

$$\boldsymbol{a} = \begin{bmatrix} a_x \\ a_y \\ a_z \end{bmatrix} \quad \boldsymbol{\omega} = \begin{bmatrix} \omega_x \\ \omega_y \\ \omega_z \end{bmatrix} \tag{8}$$

denote specific outputs. ∇ and $\boldsymbol{\varepsilon}$ represent initial bias error, and $\boldsymbol{W^a}$ and $\boldsymbol{W^\omega}$ are zero mean Gaussian white noise generally. Therefore, (4) is transformed into the airspeed kinematics equation

$$\begin{bmatrix} \dot{u} \\ \dot{v} \\ \dot{w} \end{bmatrix} = \begin{bmatrix} 0 & \omega_z & -\omega_y \\ -\omega_z & 0 & \omega_x \\ \omega_y & -\omega_x & 0 \end{bmatrix} \begin{bmatrix} u \\ v \\ w \end{bmatrix} + C_n^b \begin{bmatrix} 0 \\ 0 \\ g \end{bmatrix} + \begin{bmatrix} a_x \\ a_y \\ a_z \end{bmatrix}. \quad (9)$$

From (9), uncertainties of this model are input measurements from inertial sensors and attitude angles. Based on the derived equation of INS, an INS/GPS integrated system is used to estimate the attitude angles and bias error of inertial sensors. A nonlinear strap-down INS error model in [17] is considered in the following:

$$\begin{cases} \delta\dot{\boldsymbol{\Phi}} = (I - C_n^c)\boldsymbol{\omega}_{\text{in}}^n + \delta\boldsymbol{\omega}_{\text{in}}^n + C_b^n\boldsymbol{\varepsilon} \\ \delta\dot{\mathbf{v}} = (I - C_n^c)C_b^n\boldsymbol{a} \\ \qquad -\delta\left[\left(2\boldsymbol{\omega}_{ie}^n + \boldsymbol{\omega}_{en}^n\right) \times \mathbf{v}\right] + C_b^n\nabla \\ \delta\dot{\mathbf{p}} = \delta\mathbf{v} + \rho \times \delta\mathbf{p} \end{cases} \quad (10)$$

where the prefix δ stands for the error between the real value and the value computed by IMU. $\mathbf{v} = [v_N \ v_E \ v_D]^T$ denotes the ground velocity. $\mathbf{p} = [L \ \lambda \ h]^T$ represents the position in the navigation frame, and L, λ, and h stand for the latitude, longitude, and height, respectively. C_n^c describes a small rotation of the navigation frame computed (c frame) by the INS relative to the true navigation frame. $\boldsymbol{\omega}_{ie}^n = [0 \ \omega_e \cos L \ \omega_e \sin L]^T$ denotes the local Earth rotation rate vector in the navigation frame; $\boldsymbol{\omega}_{\text{in}}^n = [-\dot{L} \ \dot{\lambda}\cos L + \omega_e \cos L \ \dot{\lambda}\sin L + \omega_e \sin L]^T$ is the rotation velocity of the navigation frame n relative to the inertial frame i expressed in the n frame; $\boldsymbol{\omega}_{en}^n = \boldsymbol{\omega}_{ie}^n - \boldsymbol{\omega}_{\text{in}}^n$, $\dot{L} = (v_N/(R+h))$, and $\dot{\lambda} = (v_E \sec L/(R+h))$; R is the Earth's radius; and $\rho = [-\dot{L} \ \dot{\lambda}\cos L \ -\dot{\lambda}\sin L]^T$.

Note that these state dynamics (9) and (10) are only derived from kinematics and do not depend on the specific parameters of the aircraft model, i.e., these equations are valid for any aircraft. IMU measurements can be estimated based on the INS error model, because only the uncertainty of the derived equation is known.

Due to the random nature of wind, e.g., turbulence, it is challenging to predict the behavior of the local wind field dynamics. Therefore, the wind velocity state dynamics are modeled as a random walk process

$$\dot{\boldsymbol{\mu}}(t) = \begin{bmatrix} \dot{\mu}_x(t) \\ \dot{\mu}_y(t) \\ \dot{\mu}_z(t) \end{bmatrix} = \boldsymbol{W^\mu}(t) \quad (11)$$

where $\boldsymbol{W^\mu}(t)$ is zero mean Gaussian white noise.

Based on (9)–(11), the state-space system is formulated with the following state vector $\mathbf{x}$ and input vector $\mathbf{u}$:

$$\begin{aligned} \mathbf{x} &= [\mathbf{V}_a^T \quad \delta\boldsymbol{\Phi}^T \quad \delta\mathbf{v}^T \quad \mathbf{p}^T \quad \boldsymbol{\mu}^T \quad \nabla^T \quad \boldsymbol{\varepsilon}^T]^T \\ \mathbf{u} &= [\boldsymbol{a}^T \quad \boldsymbol{\omega}^T]^T. \end{aligned} \quad (12)$$

The process noise vector is represented by three components for accelerations, angular rates, and wind velocity

$$\mathbf{w}(t) = \begin{bmatrix} \boldsymbol{W^a}(t) \\ \boldsymbol{W^\omega}(t) \\ \boldsymbol{W^\mu}(t) \end{bmatrix}. \quad (13)$$

As derived, the state equations are given in a continuous-time nonlinear state-space format

$$\dot{\mathbf{x}}(t) = \mathbf{f}_c(\mathbf{x}(t), \mathbf{u}(t), \mathbf{w}(t)) \quad (14)$$

where $\mathbf{f}_c$ is the nonlinear continuous-time state transition function.

Next, the output equations are defined. A GPS provides the aircraft velocity relative to the ground in the NED frame. Wind velocity can readily be computed from the wind triangle. Using this relationship, the body-axis velocity components can be rotated into the NED frame and corrected for wind by [18]

$$\mathbf{v}_{\text{gps}} = \begin{bmatrix} v_N \\ v_E \\ v_D \end{bmatrix} = C_b^n \begin{bmatrix} u \\ v \\ w \end{bmatrix} + \begin{bmatrix} \mu_x \\ \mu_y \\ \mu_z \end{bmatrix}. \quad (15)$$

Note that the estimation of the wind velocity is necessary to relate ground velocity to airspeed, which is why the wind velocity components are considered as states. The angle of attack and the sideslip angle are calculated from the body-axis velocity components

$$\begin{aligned} \alpha(t) &= \tan^{-1}\left(\frac{w(t)}{u(t)}\right) \\ \beta(t) &= \sin^{-1}\left(\frac{v(t)}{\sqrt{u(t)^2 + v(t)^2 + w(t)^2}}\right). \end{aligned} \quad (16)$$

As usual, one can regard the differences between the output of INS and the output of GPS as the measurement output of the INS/GPS integrated system to estimate the attitude angles and inertial sensor errors

$$\begin{aligned} \delta\mathbf{v} &= \mathbf{v}_{\text{ins}} - \mathbf{v}_{\text{gps}} \\ \delta\mathbf{p} &= \mathbf{p}_{\text{ins}} - \mathbf{p}_{\text{gps}}. \end{aligned} \quad (17)$$

Using these signals, the output vector $\mathbf{y}$ is as follows:

$$\mathbf{y}(t) = \left[\mathbf{v}_{\text{gps}}^T \quad \alpha \quad \beta \quad \delta\mathbf{v}^T \quad \delta\mathbf{p}^T\right]^T. \quad (18)$$

Using these relationships (15)–(17), the output equations are defined by

$$\mathbf{y}(t) = \mathbf{h}(\mathbf{x}(t)) + \mathbf{D}(t)\mathbf{d}(t) \quad (19)$$

where

$$\mathbf{d}(t) = \begin{bmatrix} d^\alpha \\ d^\beta \\ \mathbf{d}^{\mathbf{V}_a} \\ \mathbf{d}^{\mathbf{p}} \end{bmatrix} \quad \mathbf{D}(t) = \begin{bmatrix} 0 & 0 & \mathbf{I}_{3\times3} & \mathbf{0}_{3\times3} \\ 1 & 0 & \mathbf{0}_{3\times3} & \mathbf{0}_{3\times3} \\ 0 & 1 & \mathbf{0}_{3\times3} & \mathbf{0}_{3\times3} \\ 0 & 0 & \mathbf{I}_{3\times3} & \mathbf{0}_{3\times3} \\ 0 & 0 & \mathbf{0}_{3\times3} & \mathbf{I}_{3\times3} \end{bmatrix}. \quad (20)$$

B. Observability Analysis

Observability provides an understanding of how well states of a system can be inferred from the system output measurements. Before the airspeed estimation, we compute the observability matrix of the system describing the airspeed estimation and prove that it is full rank. The system describing the UAV airspeed and wind velocity given ground velocity measurements is nonlinear. Therefore, tests designed for linear time-invariant systems [19] cannot be used for examining its observability. Instead, we hereafter employ the observability rank criterion based on Lie derivatives [20] to determine the conditions under which this system is locally weakly observable.

First, we give the dimension reduction of the system for the convenient of observability analysis. Equation (9) shows the characteristic of airspeed kinematics, where angular rate and acceleration are regarded as known inputs provided by INS. Meanwhile, attitude angles, i.e., C_n^b, need to be estimated. This paper uses INS/GPS integrated system to estimate the accurate attitude based on (10) and (17). In other words, INS/GPS integrated system can be regarded as a single "sensor," which provides the complete attitude information independently [17]. Meanwhile, [22] gave the observability analysis about INS/GPS system and the conclusion is acceptable for this paper. That is to say, we can regard attitude angles and their direction cosine matrix as known inputs and only consider the system as follows:

$$\dot{\mathbf{x}}_1 = \begin{bmatrix} \dot{u} \\ \dot{v} \\ \dot{w} \\ \dot{\mu}_x \\ \dot{\mu}_y \\ \dot{\mu}_z \end{bmatrix} = \begin{bmatrix} -\lfloor \boldsymbol{\omega}\times \rfloor & \mathbf{0}_{3\times3} \\ \mathbf{0}_{3\times3} & \mathbf{0}_{3\times3} \end{bmatrix} \begin{bmatrix} u \\ v \\ w \\ \mu_x \\ \mu_y \\ \mu_z \end{bmatrix} + \begin{bmatrix} C_n^b \\ \mathbf{0}_{3\times3} \end{bmatrix} \begin{bmatrix} 0 \\ 0 \\ g \end{bmatrix} + \begin{bmatrix} \mathbf{I}_{3\times3} \\ \mathbf{0}_{3\times3} \end{bmatrix} \begin{bmatrix} a_x \\ a_y \\ a_z \end{bmatrix}. \quad (21)$$

We rearrange the nonlinear kinematic equation in the following convenient form for computing the Lie derivatives based on [19]:

$$\begin{bmatrix} \dot{u} \\ \dot{v} \\ \dot{w} \\ \dot{\mu}_x \\ \dot{\mu}_y \\ \dot{\mu}_z \end{bmatrix} = \begin{bmatrix} \mathbf{I}_{3\times3} \\ \mathbf{0}_{3\times3} \end{bmatrix} \begin{bmatrix} a_x - g\sin\theta \\ a_y + g\cos\theta\sin\phi \\ a_z + g\cos\theta\cos\phi \end{bmatrix} + \begin{bmatrix} \lfloor \mathbf{V}_a\times \rfloor \\ \mathbf{0}_{3\times3} \end{bmatrix} \begin{bmatrix} \omega_x \\ \omega_y \\ \omega_z \end{bmatrix}. \quad (22)$$

Let

$$\mathbf{f}_1 = \begin{bmatrix} \mathbf{I}_{3\times3} \\ \mathbf{0}_{3\times3} \end{bmatrix} \quad \mathbf{u}_1 = \begin{bmatrix} a_x - g\sin\theta \\ a_y + g\cos\theta\sin\phi \\ a_z + g\cos\theta\cos\phi \end{bmatrix} \quad (23)$$

and

$$\mathbf{f}_2 = \begin{bmatrix} \lfloor \mathbf{V}_a\times \rfloor \\ \mathbf{0}_{3\times3} \end{bmatrix} \quad \mathbf{u}_2 = \begin{bmatrix} \omega_x \\ \omega_y \\ \omega_z \end{bmatrix} \quad (24)$$

where

$$\lfloor \mathbf{V}_a \rfloor = \begin{bmatrix} 0 & -w & v \\ w & 0 & -u \\ -v & u & 0 \end{bmatrix} \quad (25)$$

where $\lfloor \boldsymbol{\omega}\times \rfloor$ is the same form with $\lfloor \mathbf{V}_a \rfloor$.

In order to preserve the clarity of presentation, the measurement function can be divided into three parts

$$\begin{aligned} \mathbf{V}_{\text{gps}}(t) &= \mathbf{h}_1(\mathbf{x}) = \begin{bmatrix} C_b^n & \mathbf{I}_{3\times3} \end{bmatrix} \cdot \mathbf{x}_1(t) \\ \alpha(t) &= h_2(\mathbf{x}) = \tan^{-1}\left(\frac{w(t)}{u(t)}\right) \\ \beta(t) &= h_3(\mathbf{x}) = \sin^{-1}\left(\frac{v(t)}{\sqrt{u(t)^2 + v(t)^2 + w(t)^2}}\right). \end{aligned} \quad (26)$$

In the remaining of this section, we prove that the system described in (22) and (26) is observable by computing among the candidate zeroth-, first-, second-, and third-order Lie derivative of $\mathbf{h} = [\mathbf{h}_1^T h_2 h_3]^T$, the ones whose gradients ensure that the observability matrix $\mathcal{O}$ is full rank.

1) *Zeroth-Order Lie Derivatives($\mathfrak{L}^0\boldsymbol{h}$)*:

$$\begin{aligned} \mathfrak{L}^0\mathbf{h}_1 &= \mathbf{h}_1 = \begin{bmatrix} C_b^n & \mathbf{I}_{3\times3} \end{bmatrix} \cdot \mathbf{x}_1 \\ \mathfrak{L}^0 h_2 &= h_2 = \tan^{-1}\left(\frac{w}{u}\right) \\ \mathfrak{L}^0 h_3 &= h_3 = \sin^{-1}\left(\frac{v}{\sqrt{u^2 + v^2 + w^2}}\right). \end{aligned} \quad (27)$$

Therefore, the gradients of the zeroth-order Lie derivatives are exactly the same as the Jacobians of the corresponding measurement functions

$$\nabla\mathfrak{L}^0\mathbf{h} = \begin{bmatrix} C_b^n & \mathbf{I}_{3\times3} \\ \mathbf{X}_1 & \mathbf{0}_{2\times3} \end{bmatrix} \quad (28)$$

where

$$\mathbf{X}_1 = \begin{bmatrix} \dfrac{-w}{u^2 + w^2} & 0 & \dfrac{u}{u^2 + w^2} \\ \dfrac{-uv}{V^2\sqrt{u^2 + w^2}} & \dfrac{u^2 + w^2}{V^2\sqrt{u^2 + w^2}} & \dfrac{-vw}{V^2\sqrt{u^2 + w^2}} \end{bmatrix}$$

where $V^2 = u^2 + v^2 + w^2$.

2) *First-Order Lie Derivatives($\mathfrak{L}_{f_1}^1\boldsymbol{h}$: $\mathfrak{L}_{f_2}^1\boldsymbol{h}$)*:

$$\begin{aligned} \mathfrak{L}_{\mathbf{f}_1}^1\mathbf{h} &= \nabla\mathfrak{L}^0\mathbf{h}\cdot\mathbf{f}_1 = \begin{bmatrix} C_b^n \\ \mathbf{X}_1 \end{bmatrix} \\ \mathfrak{L}_{\mathbf{f}_2}^1\mathbf{h} &= \nabla\mathfrak{L}^0\mathbf{h}\cdot\mathbf{f}_2 = \begin{bmatrix} C_b^n\cdot\lfloor \mathbf{V}\times \rfloor \\ \mathbf{X}_2 \end{bmatrix} \end{aligned} \quad (29)$$

with gradients

$$\nabla\mathfrak{L}^1_{\mathbf{f}_1}\mathbf{h} = \begin{bmatrix}\boldsymbol{\Gamma}_1\\ \boldsymbol{\Gamma}_2\\ \boldsymbol{\Gamma}_3\end{bmatrix} \quad \nabla\mathfrak{L}^1_{\mathbf{f}_2}\mathbf{h} = \begin{bmatrix}\boldsymbol{\gamma}_1\\ \boldsymbol{\gamma}_2\\ \boldsymbol{\gamma}_3\end{bmatrix}$$
$$\boldsymbol{\Gamma}_i = \frac{\partial}{\partial\mathbf{x}}\left[(\mathfrak{L}^1_{\mathbf{f}_1}\mathbf{h})\mathbf{e}_i\right] \quad \boldsymbol{\gamma}_i = \frac{\partial}{\partial\mathbf{x}}\left[(\mathfrak{L}^1_{\mathbf{f}_2}\mathbf{h})\mathbf{e}_i\right]$$
$$\boldsymbol{\Gamma}_1 = \begin{bmatrix}\mathbf{0}_{3\times3} & \mathbf{0}_{3\times3}\\ \mathbf{X}_3 & \mathbf{0}_{2\times3}\end{bmatrix}$$
$$\mathbf{X}_3 = \begin{bmatrix}\dfrac{2wu}{(u^2+w^2)^2} & 0 & \dfrac{w^2-u^2}{(u^2+w^2)^2}\\ * & * & *\end{bmatrix}. \quad (30)$$

In these last expressions, $*$, $\mathbf{X}_2$, and $\mathbf{X}_3$ are the matrices of appropriate dimensions, which, regardless of their values, will be eliminated in the following derivations; hence, they need not be computed explicitly.

We end the computation of higher order Lie derivative due to the rows of $\nabla\mathfrak{L}^1_{\mathbf{f}_1}\mathbf{h}$ and $\nabla\mathfrak{L}^1_{\mathbf{f}_2}\mathbf{h}$ that are linearly dependent with C^b_n. At the same time, we can give the observability matrix

$$\mathcal{O} = \begin{bmatrix}\nabla\mathfrak{L}^0\mathbf{h}\\ \nabla\mathfrak{L}^1_{\mathbf{f}_1}\mathbf{h}\\ \nabla\mathfrak{L}^1_{\mathbf{f}_2}\mathbf{h}\end{bmatrix} = \begin{bmatrix}\nabla\mathfrak{L}^0\mathbf{h}\\ \boldsymbol{\Gamma}_1\\ \boldsymbol{\Gamma}_2\\ \boldsymbol{\Gamma}_3\\ \boldsymbol{\gamma}_1\\ \boldsymbol{\gamma}_2\\ \boldsymbol{\gamma}_3\end{bmatrix} = \begin{bmatrix}C^n_b & \mathbf{I}_{3\times3}\\ \mathbf{X}_1 & \mathbf{0}_{2\times3}\\ \mathbf{0}_{3\times3} & \mathbf{0}_{3\times3}\\ \mathbf{X}_3 & \mathbf{0}_{2\times3}\\ \mathbf{0}_{3\times3} & \mathbf{0}_{3\times3}\\ * & *\end{bmatrix}. \quad (31)$$

If the observability matrix (31) of the nonlinear system defined in (22) is full rank, then the system is locally weakly observable.

Lemma 1: The matrix

$$\mathcal{O}_1 = \begin{bmatrix}C^n_b & \mathbf{I}_{3\times3}\\ \mathbf{X}_4 & \mathbf{0}_{3\times3}\end{bmatrix} \quad (32)$$

formed by the first five rows and the ninth row of $\mathcal{O}$. The matrix $\mathcal{O}_1$ described by (32) is full rank if $\mathbf{X}_4$ is full rank

$$\mathbf{X}_4 = \begin{bmatrix}\dfrac{-w}{u^2+w^2} & 0 & \dfrac{u}{u^2+w^2}\\ \dfrac{-uv}{V^2\sqrt{u^2+w^2}} & \dfrac{u^2+w^2}{V^2\sqrt{u^2+w^2}} & \dfrac{-vw}{V^2\sqrt{u^2+w^2}}\\ \dfrac{2wu}{(u^2+w^2)^2} & 0 & \dfrac{w^2-u^2}{(u^2+w^2)^2}\end{bmatrix}. \quad (33)$$

It is obvious that $\mathbf{X}_4$ is full rank. Based on [21, Th. 1], the observability matrix (31) is full rank when attitude angles can be provided from the INS/GPS system. References [26] and [27] analyzed the observability of a fused INS/GPS integrated system. For constant turn maneuvers, it is shown that at least two more modes are instantaneously observable, which are the attitude angles. Moreover, the azimuth angle is less observable compared with the tilt angles. Therefore, the system described in (22) and (26) is locally observable during nonconstant axial accelerating maneuvers.

C. Estimation Framework

For the engineering application, the discrete time systems of this model are needed. During a short period of sampling time T_s, we approximate the nonlinear model (14) and (19) in the form of a discrete time linear state-space model

$$\begin{aligned}\mathbf{x}_k &= \mathbf{f}(\mathbf{x}_{k-1}, \mathbf{u}_{k-1}, \mathbf{w}_{k-1})\\ \mathbf{y}_k &= \mathbf{h}(\mathbf{x}_k) + \mathbf{D}_k\mathbf{d}_k.\end{aligned} \quad (34)$$

Clearly, for the nonlinear system, the process and measurement noise covariance are considered to be uncorrelated, white, and Gaussian with zero mean and known covariance matrices $\mathbf{Q}$ and $\mathbf{R}$ as in

$$\mathbf{Q}_k = E\left[\mathbf{w}_k\mathbf{w}_k^T\right] \quad \mathbf{R}_k = E\left[\mathbf{d}_k\mathbf{d}_k^T\right]. \quad (35)$$

Since the system dynamics of the proposed method are simple, the application of the EKF to the airspeed estimation is straightforward. A clearer explanation of EKF is shown.

1) Perform the time update of the state estimate and estimation-error covariance as follows:

$$\begin{aligned}\hat{\mathbf{x}}_{k,k-1} &= \mathbf{f}_{k-1}(\hat{\mathbf{x}}_{k-1,k-1}, \mathbf{u}_{k-1}, 0)\\ \mathbf{P}_{k,k-1} &= F_{k-1}\mathbf{P}_{k-1,k-1}F^T_{k-1} + L_{k-1}\mathbf{Q}_{k-1}L^T_{k-1}\end{aligned} \quad (36)$$

where

$$F_{k-1} = \frac{\partial\mathbf{f}_{k-1}}{\partial\mathbf{x}}|_{\hat{\mathbf{x}}_{k-1,k-1}} \quad L_{k-1} = \frac{\partial\mathbf{f}_{k-1}}{\partial\mathbf{w}}|_{\hat{\mathbf{x}}_{k-1,k-1}}. \quad (37)$$

2) At time k, incorporate the measurement $\mathbf{y}_k$ into the state estimate and estimation covariance as follows:

$$\begin{aligned}K_k &= \mathbf{P}_{k,k-1}H^T_k\left(H_k\mathbf{P}_{k,k-1}H^T_k + \mathbf{D}_k\mathbf{R}_k\mathbf{D}^T_k\right)^{-1}\\ \hat{\mathbf{x}}_{k,k} &= \hat{\mathbf{x}}_{k,k-1} + K_k(\mathbf{y}_k - \mathbf{h}(\hat{\mathbf{x}}_{k,k-1}))\\ \mathbf{P}_{k,k} &= (I - K_kH_k)\mathbf{P}_{k,k-1}(I - K_kH_k)^T\\ &\quad + K_k\mathbf{D}_k\mathbf{R}_k\mathbf{D}^T_kK^T_k\end{aligned} \quad (38)$$

where

$$H_k = \frac{\partial\mathbf{h}_k}{\partial\mathbf{x}}|_{\hat{\mathbf{x}}_{k,k-1}}. \quad (39)$$

IV. Fault Diagnosis Scheme

A. Sensors Health Monitoring

This paper uses the difference between the virtual "airspeed," estimated using IMU, GPS, and wind vanes, and the airspeed measurement provided by pitot tube to indicate the fault information of the pitot tube. Therefore, these sensors used for the airspeed estimation need to be constantly monitored whether they are reliable. For the EKF estimation of airspeed, define the residual as

$$\tilde{\mathbf{y}}(k) = \mathbf{y}(k) - \hat{\mathbf{y}}(k) = \mathbf{y}(k) - \mathbf{h}(\hat{\mathbf{x}}_{k,k}). \quad (40)$$

Note that the output $\mathbf{y}(k)$ did not include the information of the pitot tube. If the used sensors are healthy, the following result is easily achieved:

$$\tilde{\mathbf{y}}(k) \sim N(0, R_{\tilde{\mathbf{y}}}). \quad (41)$$

Introduce the residual evaluation

$$J_N(k) = \frac{1}{N+1} \sum_{j=k-N}^{k} \tilde{\mathbf{y}}^T(j) R_{\tilde{\mathbf{y}}}^{-1}(j) \tilde{\mathbf{y}}(j). \tag{42}$$

Based on (41), $J_N(k)$ follows a central χ^2 distribution with 11 degrees of freedom. Therefore, we can use $J_N(k)$ as an evaluation function and monitor the status of the sensors. Choose a false alarm rate (FAR) ε; then, the threshold can be determined based on the χ^2 distribution

$$J_{th} = \chi^2_{11,\varepsilon}. \tag{43}$$

Finally, the health monitoring can be performed as the following statistical χ^2 test:

$$\begin{cases} \text{if} \quad J_N(k) < J_{\text{th}}, & \text{sensors work properly} \\ \text{if} \quad J_N(k) \geq J_{\text{th}}, & \text{sensors work incorrectly.} \end{cases} \tag{44}$$

When the evaluation function $J_N(k)$ is under the threshold J_{th}, the results of the airspeed estimation is credible for the FD process. Only by healthy sensors can this approach continues the airspeed sensor FD. In order to ensure the reliability of this approach, the value ε should be appropriate.

B. Airspeed Sensor Fault Detection

Since the pitot tube was installed in alignment with the x-direction of the aircraft, it measures the x-component of the airspeed u. To correct this, the angle of attack α and the sideslip angle β are utilized [23], resulting in the following expression for the airspeed:

$$V_m(k) = \frac{V_{\text{pitot}}(k)}{\cos\alpha(k)\cos\beta(k)} \tag{45}$$

where $V_m(k)$ is the absolute value of the physical airspeed and $V_{\text{pitot}}(k)$ is the x-axis component of $V_m(k)$ calculated by ADS. This value is used only as a comparison reference for validating the analytical redundancy approach. It is not used in the filtering process. The estimated values of $\hat{u}, \hat{v}$, and $\hat{w}$ from the filter are used to determine the estimated airspeed, as in

$$\hat{V}(k) = \sqrt{\hat{u}^2(k) + \hat{v}^2(k) + \hat{w}^2(k)}. \tag{46}$$

The residual signal $r(k)$ for the pitot tube is defined as

$$r(k) = V_m(k) - \hat{V}(k). \tag{47}$$

The FD procedure is designed to determine whether the observed changes in the residual signal $r(k)$ can be justified in terms of the disturbance (measurement noise) or modeling uncertainty. In Fig. 3, the histogram of the residual from a real flight experiment is shown. We choose 20 000 points of $r(k)$. The residual has been made to have a zero mean. The histogram shows that the noise on residual follows a normal distribution with a general form of:

$$p(r;\mu,\sigma) = \frac{1}{\sigma\sqrt{2\pi}} e^{-\frac{(r-\mu)^2}{2\sigma^2}}. \tag{48}$$

The purpose of FD is typically to detect both the positive and negative changes in the amplitude in the mean value of the residual signal $r(k)$ caused by the occurrence of a fault. In this paper, it is convenient to introduce the following hypotheses about the residuals $r(1)\cdots r(k)$ for $1 \leq j \leq k$:

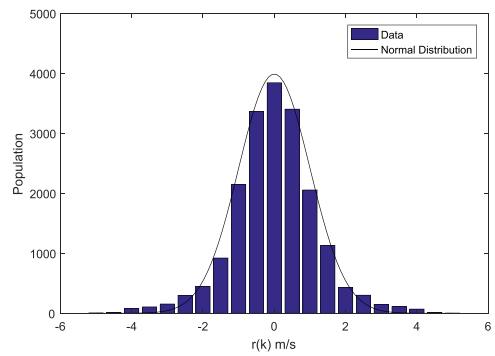

Fig. 3. Residual characteristics.

$$\begin{aligned} H_0 &: \quad \mu = \mu_0 \quad \text{for} \quad 1 \leq i \leq k \\ H_j &: \begin{cases} \mu = \mu_0 & \text{for} \quad 1 \leq i \leq j-1 \\ \mu = \mu_1 & \text{for} \quad j \leq i \leq k. \end{cases} \end{aligned} \tag{49}$$

The likelihood ratio between hypotheses H_0 and H_j is

$$\Lambda_1^k(j) = \frac{\prod_{i=1}^{j-1} p_{\mu_0}(r_i) \prod_{i=j}^{k} p_{\mu_1}(r_i)}{\prod_{i=1}^{k} p_{\mu_0}(r_i)} \tag{50}$$

where $\prod_{i=1}^{0} = 1$. Thus, the log-likelihood ratio is

$$Z_j^k = \sum_{i=j}^{k} ln \frac{p_{\mu_1}(r_i)}{p_{\mu_0}(r_i)}. \tag{51}$$

As mentioned in [28], the typical behavior of the log-likelihood ratio Z_j^k shows a negative drift before a change and a positive drift after change. Therefore, the relevant information regarding the change lies in the difference between the value of the log-likelihood ratio and its current minimum value. The corresponding decision rule is to compare this difference with a threshold as follows:

$$S^+(k) = Z_1^k - \min_{1<j<k} Z_1^j \geq h \tag{52}$$

where

$$Z_1^j = \frac{\mu_1 - \mu_0}{\sigma^2} \sum_{i=1}^{j} (r(k) - \frac{\mu_1 + \mu_0}{2}) \tag{53}$$

and h is the threshold. In the second formulation

$$S^+(k) = \left[S^+(k-1) + \frac{\mu_1 - \mu_0}{\sigma^2} (r(k) - \frac{\mu_1 + \mu_0}{2}) \right]^+ \tag{54}$$

where $[x]^+ = \sup(0, x)$. As long as the decision is taken in favor of H_0, the sampling and test continue. Sampling is stopped after the first of observations for which the decision is taken in favor of H_j.

This is the well-known filter used for the detection of moderate persistent shifts in the mean value of residuals, named the CUSUM filter [28]. In this paper, we limited the analysis to faults with positive amplitudes, that is, following

the fault, the mean value of the residual is expected to be $\mu_1 = \mu_0 + \tau$. The values of the parameter τ (that is, the value of the expected fault amplitude) strongly affect the sensitivity of the CUSUM signals to faults having generic amplitudes. In this paper, a baseline value was fixed for the fault amplitude that is equal to the variance of the estimation error for the airspeed channel, that is, $\tau = \sigma_0$. The CUSUM filter is defined by the following equation [29]:

$$S^+(k) = \sup\left(0, S^+(k-1) - \frac{\tau(\tau - 2r(k))}{2\sigma_0^2}\right). \tag{55}$$

The FD threshold for the CUSUM signal $S^+(k)$ was selected as a compromise between the need for a fast FD and the need for low FARs. An acceptable tradeoff was found by setting the threshold equal to 1.5 times the maximum value of the CUSUM signal observed in fault-free conditions for a validation simulated flight

$$h = 1.5 \cdot \max(S^+(k)). \tag{56}$$

Based on (44) and (55), the FD logic of airspeed sensor can be expressed as follows:

$$\begin{cases} \text{if} \quad J_N(k) \quad \geq J_{\text{th}} \text{sensors work incorrectly} \\ \text{if} \quad J_N(k) \quad < J_{\text{th}}, S^+(k) < h \quad \text{no fault} \\ \text{if} \quad J_N(k) \quad < J_{\text{th}}, S^+(k) > h \quad \text{fault alarm.} \end{cases} \tag{57}$$

When $J_N(k)$ exceeds the threshold J_{th}, the sensors used in airspeed estimation is abnormal and the FD process should be suspended; when $J_N(k)$ is under the threshold J_{th} and $S^+(k)$ also is under the threshold h, there is no fault in the airspeed sensor; only when $J_N(k)$ is under the threshold J_{th} and $S^+(k)$ exceeds the threshold h, there is a fault in the airspeed sensor. This logical structure of two residuals guarantees the reliability and accuracy of the airspeed sensor FD.

V. Experiment

A. Ultra Stick 25e Research Platform

The research platform used in this paper is the Ultra Stick 25e UAV. This platform consists of a fleet of three UAVs that were designed, manufactured, and instrumented by researchers of the Uninhabited Aerial Vehicle Laboratories at the University of Minnesota for various research topics, including formation flight, fault-tolerant flight control, and sensor fusion. The UAV named "Thor" was utilized for this paper, as shown in Fig. 4.

The onboard avionics system, shown in Fig. 5, features a GlobalSat EM-406A GPS receiver with a 5-m circular error probable for position measurements and 0.1-m/s rms accuracy for velocity, as well as an Analog Devices iSensor ADIS16405 IMU, accelerometers with 50-mg initial bias error and 9-mg rms noise, and gyroscopes with 3°/s initial bias error and 0.9°/s rms output noise. Additionally, the platform features a Goodrich Inc., 0858 mini five-hole probe that provides measurements of angle of attack and sideslip with 0.2° measurement accuracy in addition to static and dynamic pressure measurements from a pitot tube.

Fig. 4. Ultra Stick 25e.

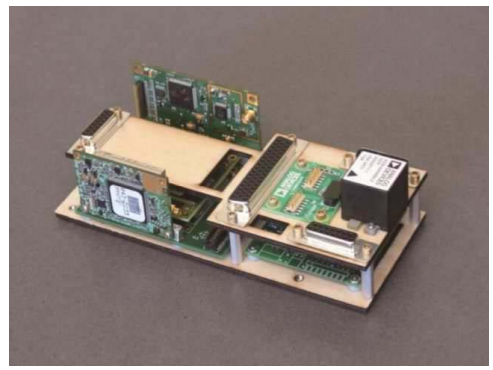

Fig. 5. Ultra Stick 25e avionics system.

B. Airspeed Estimation

To implement a nonlinear Kalman filter, the process and measurement noise covariance matrices $\mathbf{Q}$ and $\mathbf{R}$ must be determined. These matrices were determined using the sensor specifications and were used as constants throughout the filtering.

One flight from the Thor aircraft and one flight from the Faser aircraft were selected to illustrate the effectiveness of airspeed estimation under different situations. The Faser aircraft is based on the Ultra Stick 120e platform and has a larger size than Thor but the same sensors as Thor. Figs. 6 and 7 show the trajectories and estimation results of each flight.

The Thor flight was conducted to test the waypoint tracking algorithm with a more precise waypoint tolerance of 10 m. A waypoint pattern consisting of five points was used, and the algorithm and controller performed very well. The Faser flight was an altitude/airspeed tracking performance test. In each of the two figures, the estimation of the airspeed is shown with the reference airspeed from the pitot tube. It is shown that the airspeed estimation performance is independent of the pitot tube. From these average results, these two results both provided accurate estimations of airspeed from different UAVs. The quantitative results for each set of flight data from the Thor and the Faser aircraft are summarized in Table I. The statistical results of the analyses are quantified in terms of the mean μ_0 and standard deviation σ_0 of the airspeed estimation error with respect to the independent pitot tube

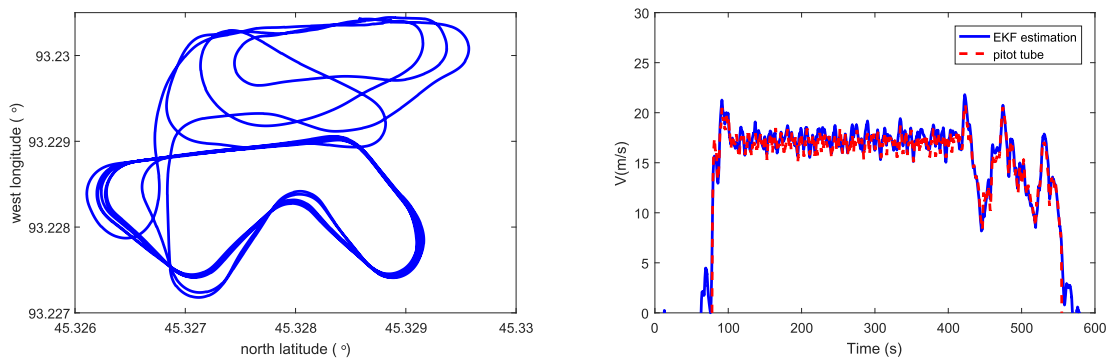

Fig. 6. Thor flight trajectory and airspeed estimation.

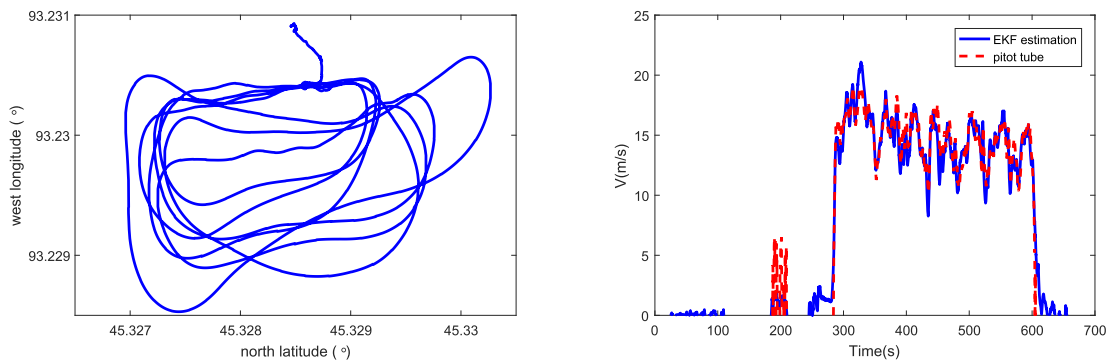

Fig. 7. Faser flight trajectory and airspeed estimation.

TABLE I
AIRSPEED AND WIND VELOCITY ESTIMATION RESULTS

Aircraft	$\mu_0(\triangle$ V)[m/s]	σ_0 ($\triangle$ V)[m/s]	mean(μ)[m/s]
Thor	0.3056	0.6015	1.3682
Faser	0.1904	0.7885	1.6458

reference and mean estimated wind speed. These statistics were calculated only for in-air segments of data. Note that flights with higher levels of wind do not lead to larger standard deviation errors in airspeed estimation. This result indicates that the airspeed estimation does not heavily depend on the magnitude of wind experienced during the flight. This is also a very desirable characteristic, since it is difficult to predict future wind conditions.

Note that these two flights were from two different UAVs. Thus, this result demonstrates and validates the platform-independent effectiveness of this technique. Therefore, it can be inferred that the accuracy of the results through this approach is not linked to the aircraft dynamics model but is only a function of the sensors that are used. A major benefit of this approach is that it can be tested on one aircraft and implemented on another using the same sensors. Additionally, through some tuning, similar sensing systems can easily be adapted to fit this method.

C. Health Monitoring for Sensors

Before the fault diagnosis of the pitot tube, we should keep the other sensors outputting accurate information. Consider the χ^2 test in (42). Based on the χ^2 distribution, we choose

$$J_{\text{th}} = \chi^2_{11,0.05} = 19.6. \tag{58}$$

To illustrate the effectiveness, we add a simulated GPS velocity outlier to the Thor flight data as follows:

$$\Delta v_N(k) = \begin{cases} 3\text{m/s} & k = 200\text{s} \sim 202\text{s} \\ -3\text{m/s} & k = 202\text{s} \sim 204\text{s} \\ 3\text{m/s} & k = 204\text{s} \sim 206\text{s} \\ -3\text{m/s} & k = 206\text{s} \sim 208\text{s}. \end{cases} \tag{59}$$

Fig. 8 shows two results of the χ^2 tests. Fig. 8 (left) shows the evaluation function in the condition that the GPS velocity has outliers at 200–208 s. Fig. 8 (right) shows the evaluation function in the condition that used sensors remain in a healthy status. From Fig. 8 (left), the J_N exceeds the threshold when the fault occurs immediately. However, J_N still remains under the threshold in Fig. 8 (right). Therefore, when other sensors have no faults as in Fig. 8 (right), we can use the estimation results to implement the airspeed sensor FD.

D. Fault Detection for Airspeed Sensor

Consider the CUSUM detector in (55). Table I shows the airspeed residual results μ_0 and σ_0 of two flights. Furthermore, as explained in Section IV, the baseline value for the expected fault amplitude to be used in (55) was fixed at $\tau = \sigma_0$. We add the simulated additive fault to the airspeed from the pitot tube, and the fault amplitude is the same as ΔV from Table I.

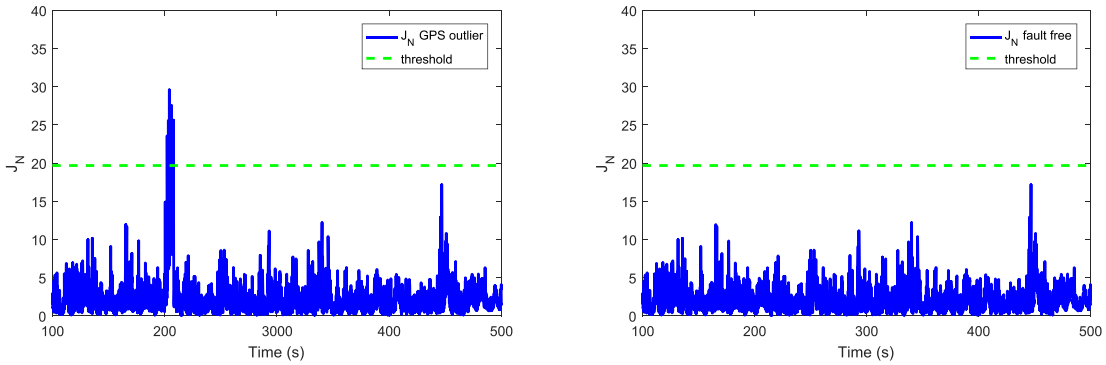

Fig. 8. χ^2 test for other sensors.

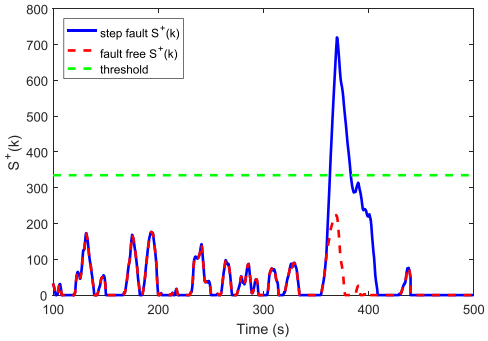

Fig. 9. Thor flight airspeed fault diagnosis.

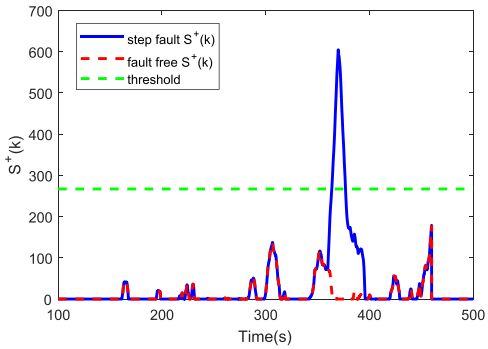

Fig. 10. Faser flight airspeed fault diagnosis.

For the Thor flight

$$\begin{aligned} A &= 0.6015\text{m/s} \\ t_f &= 360\text{s} \\ T_R &= 40\text{s}. \end{aligned} \tag{60}$$

For the Faser flight

$$\begin{aligned} A &= 0.7885\text{m/s} \\ t_f &= 360\text{s} \\ T_R &= 40\text{s}. \end{aligned} \tag{61}$$

Figs. 9 and 10 show the results of the CUSUM detector $S^+(k)$. From Figs. 9 and 10, we choose two thresholds for the CUSUM detector based on (56). For the Thor flight, we choose

$$h = 335. \tag{62}$$

For the Faser flight, we choose

$$h = 267. \tag{63}$$

As shown in Fig. 9, before $t = 360$ s, the CUSUM signal remains well below the threshold. With the chosen threshold detection, the first signs that indicate the airspeed sensor fault occurred at approximately $t = 360.2$ s according to the blue line. More importantly, this observation is approximately 0.2 s within the operator's reaction time. In Fig. 10, before $t = 360$ s, the CUSUM signal stays well below the threshold. The first signs that indicate the airspeed sensor fault occurred at approximately $t = 360.1$ s according to the blue line. From these results, we can conclude that without pitot information and dynamic parameters, this method can provide good performance for airspeed sensor FD.

VI. Conclusion

FD of the airspeed measurement system for UAVs was considered in this paper. An airspeed estimation based on a kinematic model was proposed, and a detector for airspeed was employed to detect additive step faults in the measurements of the airspeed signal. This method was verified using real data from two UAVs. The results revealed that the proposed methodology is attractive for practical applications because of its ability to detect faults.

References

[1] M. Rossi and D. Brunelli, "Autonomous gas detection and mapping with unmanned aerial vehicles," *IEEE Trans. Instrum. Meas.*, vol. 65, no. 4, pp. 765–775, Apr. 2016.

[2] C. Hajiyev and F. Caliskan, *Fault Diagnosis and Reconfiguration in Flight Control Systems*. Boston, MA, USA: Kluwer, 2003.

[3] J. C. Deckert, M. Desai, J. J. Deyst, and A. Willsky, "F-8 DFBW sensor failure identification using analytic redundancy," *IEEE Trans. Autom. Control*, vol. AC-22, no. 5, pp. 795–803, Oct. 1977.

[4] X. Liu, M. Zhong, and H. Liu, "EKF-based fault detection of unmanned aerial vehicle flight control system," *J. Shanghai Jiaotong Univ.*, vol. 49, no. 6, pp. 884–888, Jun. 2015, doi: 10.16183/j.cnki.jsjtu.2015.06.024.

[5] C. Hajiyev, "Tracy–Widom distribution based fault detection approach: Application to aircraft sensor/actuator fault detection," *ISA Trans.*, vol. 51, no. 1, pp. 189–197, Jan. 2012.

[6] P. S. Maybeck, "Multiple model adaptive algorithms for detecting and compensating sensor and actuator/surface failures in aircraft flight control systems," *Int. J. Robust Nonlin.*, vol. 9, no. 4, pp. 1051–1070, Dec. 1999.

[7] D. T. Magill, "Optimal adaptive estimation of sampled stochastic processes," *IEEE Trans. Autom. Control*, vol. AC-10, no. 4, pp. 434–439, Oct. 1965.

[8] A. Marcos, S. Ganguli, and G. J. Balas, "An application of H_∞ fault detection and isolation to a transport aircraft," *Control Eng. Pract.*, vol. 13, no. 1, pp. 105–119, Jan. 2005.

[9] M. Mattei, G. Paviglianiti, and V. Scordamaglia, "Nonlinear observers with H_∞ performance for sensor fault detection and isolation: A linear matrix inequality design procedure," *Control Eng. Pract.*, vol. 13, no. 10, pp. 1271–1281, Oct. 2005.

[10] M. L. Fravolini *et al.*, "Model-based approaches for the airspeed estimation and fault monitoring of an unmanned aerial vehicle," in *Proc. IEEE Workshop Environ. Energy Struct. Monitor. Syst. (EESMS)*, Perugia, Italy, Sep. 2012, pp. 18–23.

[11] F. Chen, R. Jiang, K. Zhang, B. Jiang, and G. Tao, "Robust backstepping sliding-mode control and observer-based fault estimation for a quadrotor UAV," *IEEE Trans. Ind. Electron.*, vol. 63, no. 8, pp. 5044–5056, Aug. 2016.

[12] M. B. Rhudy, M. L. Fravolini, Y. Gu, M. R. Napolitano, S. Gururajan, and H. Chao, "Aircraft model-independent airspeed estimation without pitot tube measurements," *IEEE Trans. Aerosp. Electron. Syst.*, vol. 51, no. 3, pp. 1980–1995, Jul. 2015.

[13] R. G. Lins, S. N. Givigi, and P. R. Kurka, "Velocity estimation for autonomous vehicles based on image analysis," *IEEE Trans. Instrum. Meas.*, vol. 65, no. 1, pp. 96–103, Jan. 2016.

[14] S. Hansen, M. Blanke, and J. Adrian, "Diagnosis of UAV pitot tube defects using statistical change detection," *IFAC Proc. Volumes*, vol. 43, no. 16, pp. 485–490, Sep. 2010.

[15] A. Cho, J. Kim, S. Lee, and C. Kee, "Wind estimation and airspeed calibration using a UAV with a single-antenna GPS receiver and pitot tube," *IEEE Trans. Aerosp. Electron. Syst.*, vol. 47, no. 1, pp. 109–117, Jan. 2011.

[16] S. Hansen and M. Blanke, "Diagnosis of airspeed measurement faults for unmanned aerial vehicles," *IEEE Trans. Aerosp. Electron. Syst.*, vol. 50, no. 1, pp. 224–239, Jan. 2014.

[17] X. Gong, R. Zhang, and J. Fang, "Application of unscented R–T–S smoothing on INS/GPS integration system post processing for airborne earth observation," *Measurement*, vol. 46, no. 3, pp. 1074–1083, Apr. 2013.

[18] J. Langelaan, N. Alley, and J. Neidhoefer, "Wind field estimation for small unmanned aerial vehicles," *J. Guid. Control Dyn.*, vol. 34, no. 4, pp. 1016–1030, Aug. 2011.

[19] P. S. Maybeck, *Stochastic Models, Estimation and Control*. New York, NY, USA: Academic, 1979.

[20] R. Hermann and A. Krener, "Nonlinear controllability and observability," *IEEE Trans. Autom. Control*, vol. AC-22, no. 5, pp. 728–740, Oct. 1977.

[21] G. Panahandeh, M. Jansson, and P. Händel, "Calibration of an IMU-camera cluster using planar mirror reflection and its observability analysis," *IEEE Trans. Instrum. Meas.*, vol. 64, no. 1, pp. 75–88, Jan. 2015.

[22] D. Goshen-Meskin and I. Y. Bar-Itzhack, "Observability analysis of piece-wise constant systems. II. Application to inertial navigation in-flight alignment," *IEEE Trans. Aerosp. Electron. Syst.*, vol. 28, no. 4, pp. 1068–1075, Oct. 1992.

[23] B. Stevens, F. Lewis, and E. Johnson, *Aircraft Control and Simulation: Dynamics, Controls Design and Autonomous Systems*. Hoboken, NJ, USA: Wiley, 2015.

[24] Q. Zhao and M. Kinnaert, "Statistical properties of CUSUM based fault detection schemes for fault tolerant control," in *Proc. 48th IEEE Conf. Decision Control (CDC) Held Jointly, 28th Chinese Control Conf.*, Shanghai, China, Dec. 2009, pp. 7831–7836.

[25] R. Collinson, *Introduction to Avionics Systems*. New York, NY, USA: Springer, 2011.

[26] I. Rhee, M. F. Abdel-Hafez, and J. L. Speyer, "Observability of an integrated GPS/INS during maneuvers," *IEEE Trans. Aerosp. Electron. Syst.*, vol. 40, no. 2, pp. 526–535, Apr. 2004.

[27] Y. Wu, H. Zhang, M. Wu, X. Hu, and D. Hu, "Observability of strapdown INS alignment: A global perspective," *IEEE Trans. Aerosp. Electron. Syst.*, vol. 40, no. 2, pp. 78–102, Apr. 2004.

[28] M. Basseville and I. Nikiforov, *Detection Abrupt Changes: Theory Application*. Englewood Cliffs, NJ, USA: Prentice-Hall, 1993.

[29] G. Campa *et al.*, "On-line learning neural networks for sensor validation for the flight control system of a B777 research scale model," *Int. J. Robust Nonlin.*, vol. 12, no. 11, pp. 987–1007, Apr. 2002.

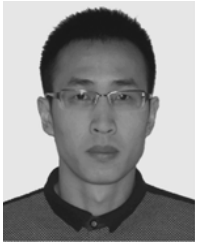

Dingfei Guo received the B.Sc. degree from Beihang University, Beijing, China, in 2011, where he is currently pursuing the Ph.D. degree.

His current research interests include the inertial technology and integrated navigation technology.

Maiying Zhong received the Ph.D. degree in control theory and control engineering from Northeastern University, Shenyang, China, in 1999.

From 2000 to 2001, she was a Research Fellow with Donghua University, Shanghai, China. She was a Professor with the School of Control Science and Engineering, Shandong University, Jinan, China, from 2002 to 2008, and was a Professor with the School of Instrumentation and Opto-electronics Engineering, Beihang University, Beijing, China, from 2009 to 2015. She is currently a Professor with the College of Electrical Engineering and Automation, Shandong University of Science and Technology, Qingdao, China. Her current research interests are in model-based fault diagnosis, fault-tolerant systems, and their applications.

Donghua Zhou (SM'99) received the B.Eng., M.Sc., and Ph.D. degrees in electrical engineering from Shanghai Jiao Tong University, Shanghai, China, in 1985, 1988, and 1990, respectively.

He was an Alexander von Humboldt Research Fellow with the University of Duisburg-Essen, Duisburg, Germany, from 1995 to 1996, and was a Visiting Scholar with Yale University, New Haven, CT, USA, from 2001 to 2002. He joined Tsinghua University in 1997, where he was a Professor and the Head of the Department of Automation from 2008 to 2015. He is currently the Vice President of the Shandong University of Science and Technology, Qingdao, China. He has authored or co-authored over 140 peer-reviewed international journal papers and six monographs in the areas of process identification, fault diagnosis, fault-tolerant control, reliability prediction, and predictive maintenance.

Dr. Zhou is a member of the IFAC Technical Committee on Fault Diagnosis and Safety of Technical Processes. He was the NOC Chair of the 6th IFAC Symposium on SAFEPROCESS 2006. He is an Associate Editor of the *Journal of Process Control* and the Vice Chairman of the Chinese Association of Automation.